Modelling flow through a permeable bed: a combined physical-numerical approach

G. Blois, G. Sambrook Smith & J. Lead
School of Geography, Earth & Environmental Sciences, University of Birmingham, United Kingdom

R. Hardy
Department of Geography Science Laboratories, Durham University, United Kingdom

J. Best
Department of Geology and Ven Te Chow Hydrosystems Laboratory, University of Illinois, United States

ABSTRACT: In this paper, a CFD code developed to model turbulent flow across the surface-subsurface interface of a high-conductivity permeable bed is validated by using experimental data collected at the scale of the individual pore space. High-resolution endoscopic PIV data are compared with numerical results for the simple model of a permeable bed comprising uniform size spheres (D = 4 cm) packed in a cubic arrangement. We present here details of both the numerical and experimental techniques combined for investigating such turbulent interstitial flow, and highlight the major issues involved in both the numerical and physical modelling.

Keywords: CFD, PIV, Porous media, Non-Darcian flow, Turbulent structure

1 INTRODUCTION

Developing numerical models capable of simulating the hydrodynamics of open-channel flows over rough and permeable beds is crucial for predicting the morphodynamic evolution of alluvial channels and the complex physical-chemical processes occurring within the subsurface (hyporheic zone) of river beds. However, most current numerical models assume that alluvial streams have an impermeable channel bed (Raudkivi, 1998). This represents a significant issue as experimental observations have shown that such assumptions are erroneous as turbulence within gravel-beds can be significant (Bencala and Walters, 1983). Thus, Darcian theory, suitable for low-conductivity porous media, should not be applied within cohesionless gravel-bed rivers. The Navier Stokes (NS) equations can be used to model flow through a porous media if the internal morphology is known. However, this is rarely the case and the complexity of the internal morphology of the bed has meant that the normal approach to this problem is to volume-average the NS equations and close them with the Hazen-Dupui-Darcy (HDD) model (Lage et al., 2002). However, if the internal morphology of the bed is known, a mass flux scaling algorithm that has been developed to include complex bed topography into a stable discretization (Lane et al., 2003 and 2004; Hardy et al., 2005) can be applied.

Even thought these models represent the state-of-the-art, they remain largely untested, and hence their reliability remains unknown. The lack of validation data is due to the fact that experimental techniques can not currently meet the significant challenges required to fully characterize the complex instantaneous turbulent patterns produced within bed pore spaces.

To meet this challenge, a novel high-resolution endoscopic particle image velocimetry (E-PIV) technique, capable of collecting data within the pore spaces of a submerged permeable bed, has been developed. The purpose of the present paper is to present the first comparison between interstitial velocity data obtained from a 3-D CFD model and this analogue experimental data. Experiments were tailored to meet the CFD requirements and to simplify the basic validation procedures.

2 PHYSICAL PROBLEM AND APPROACH

2.1 *The permeable bed model*

The exact same geometry was used for both the numerical and experimental models. In order to simplify the comparison of the results we considered a simple geometry which can be seen as the

idealisation of a flat gravel-bed. The bed was made from uniform size spheres in a regular arrangement (see Figure 1). The permeable domain, which is overlaid by a free-surface flow, is bounded underneath by an impermeable surface. The main advantage of using a regular solid matrix is that the internal morphology of the porous bed is completely known with a high level of accuracy. This gives us the confidence of geometrically matching the numerical model domain to the experimental conditions.

The flume was 2.4 m long with a rectangular cross-section (width = 0.35 m). The permeable bed comprised six horizontal layers of uniform diameter ($D = 0.04$ m) spheres giving a total bed depth $h_{bed} = 0.24$ m. Whilst the numerical code resolved the flow in the whole 3D flume domain, the experimental data were collected within a specific pore space which was located two layers underneath the surface-subsurface interface (i.e. 8 cm underneath the bed surface).
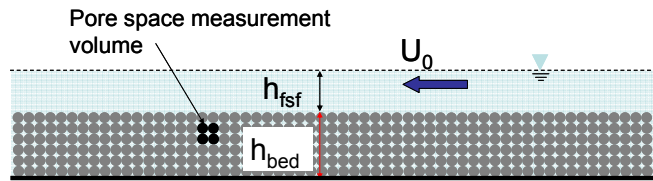

Figure 1. Schematic of the permeable bed model. The channel cross-section dimensions are: width= 0.35 m and height= 0.60 m. The pore space measurement volume is marked; this was located at 1.68 m downstream from the inlet section and (10 cm underneath the top of the spheres).

2.2 CFD model

The algorithm is based upon a mass flux scaling treatment where a structured Cartesian grid is used that is also capable of replicating the complex geometry encountered in natural gravel beds. This has been accomplished with a modification to the mass conservation equation through the development of a 5 term porosity algorithm in which: fully blocked cells are assigned a porosity of zero; fully unblocked cells are assigned a porosity of one; and faces of partly blocked cells are assigned a porosity of between 0 and 1, according to the percentage of the cell face that is blocked. This discretization is used in a standard numerical scheme that solves the full three-dimensional Navier-Stokes equations discretized using a finite-volume method. The interpolation scheme used is hybrid-upwind, where upwind differences are used in high convection areas (Peclet number > 2) and central differences are used where diffusion dominates (Peclet number < 2). Although this scheme can suffer from numerical diffusion, it is very stable. The pressure and momentum equations are coupled by applying

SIMPLEST, a variation on the SIMPLE algorithm of Patankar and Spalding (1972). The equations are closed using the RNG-$\kappa\varepsilon$ turbulence model. Finally, velocity profiles collected through UDVP data (see Figure 2) were used for an inlet boundary condition (a fixed mass boundary) while the outlet is prescribed using a fixed-pressure boundary condition where mass is allowed to enter and leave the domain.

2.3 Boundary conditions

In order to characterize the free-stream flow of the experimental model, and so provide flow boundary conditions for the numerical simulations, vertical profiles of the streamwise velocity component were measured using an array of four ultrasonic Doppler velocity profilers (UDVP). The UDVP data were used to estimate the percentage of flow moving above (Q_{stream}) and through (Q_{bed}) the bed. From these profiles, the mean free-stream velocity ($U_0 = Q_{stream}/(B*h_{fsf})$), which was used to define the open channel Reynolds number $Re = U_0 h_{fsf}/\nu$ (where ν is the kinematic viscosity), was quantified.

All experiments and simulations were conducted under steady flow boundary conditions. One experimental condition has been examined in detail for this paper. The flow depth used was $h_{fsf} = 0.06$ m while the mean free-stream velocity was $U_0 = 0.568$ m/s (Re = $3.4*10^4$).

The velocity profile shown in Figure 2 represents the mean vertical profile of the streamwise velocity component taken from the free-stream flow. This velocity profile was used as the inlet boundary condition for the numerical simulation.
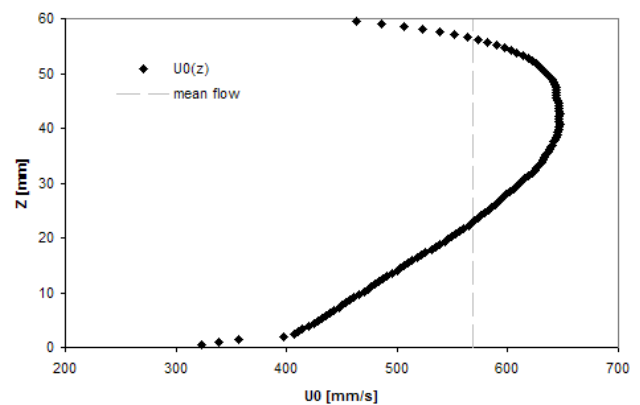

Figure 2. Vertical profile of averaged streamwise velocity component collected by UDVP in the water column and defining the free-stream flow boundary condition examined. ($h_{fsf} = 0.06$m; $U_0 = 0.568$ m/s; $Q_{tot} = 20$l/s; $Q_{stream} = 12$ l/s; Re = $3.4*10^4$)

2.4 *Experimental set-up*

Experiments were conducted in a recirculating open channel. The pore-flow was measured within the pore space measurement volume (Figure 1) by using a specially developed time-resolved endoscopic particle image velocimetry (E-PIV). The E-PIV technique consists of two endoscopes, a digital high-speed video camera and a pulsed laser source. The camera endoscope (CE) provided the optical access to the pore space while the laser endoscope (LE) directed light into the pore space (Figure 3).

Flow was imaged by connecting the CE to a high-resolution (2352*1728 pixels) digital Image-Intensified Camera. The LE was connected to a double-pulsed Nd:YAG 532 nm laser with output energy up to 120 mJ per pulse and repetition rate up to 15 Hz. A 4Gb on board camera memory allowed the collection of 500 sequential image pairs at full resolution.

In order to minimize loss of light and maximize resolution and brightness, a rod-lens based bore-scope with high transmission was used. The CE was 300 mm long with an 8 mm external diameter shaft borescope. The CE had a 0° view direction and a 67° angle of view and was connected to the camera through a 50 mm focal length Nikon lens to provide appropriate magnification of the pore space. The CE was mounted horizontally through the wall of the flume (Figure 3). Four endoscopic ports allowed quantification of the flow at different depths within the bed; the results reported herein are from the second pore space beneath the surface bed (Figure 3, port B). The distance between the end of the CE and the measurement plane was 0.04 m, thereby resulting in negligible flow perturbation, maximum image resolution and a more complete field of view in comparison to external PIV applications in beds of packed spheres.

A 0° view angle laser endoscope (LE) was used to convey the laser beam and illuminate the pore space (Figure 1a and b). The LE consisted of a 27 mm long cylindrical probe (with 12 mm external diameter). The probe terminated at a cylindrical lens (8 mm diameter) that produced a light sheet (0.5-1 mm thick) with a lateral divergence angle of approximately 26°. A spherical lens with a focal length of 300 mm was used. The laser beam is conveyed to the LE through an articulated arm. The LE probe was vertically inserted through the flume base via a customized port that allowed adjustable positioning in the horizontal plane.
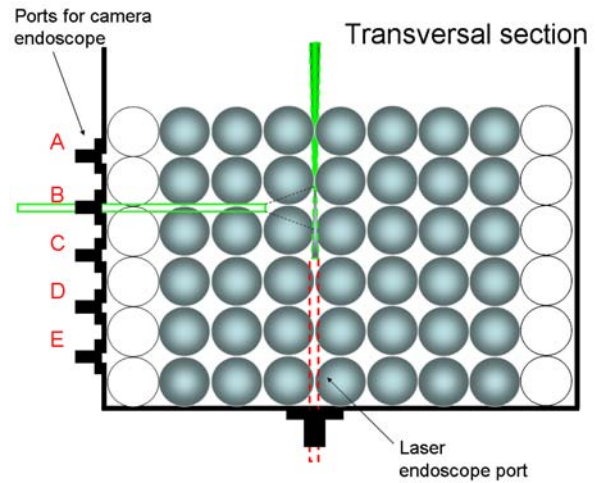

Figure 3. Endoscopic PIV set up. The figure schematically illustrates the flume cross-section and shows the endoscopes set up. The multiple camera endoscope's port system provided on the flume wall is reported in the figure; it allowed introducing the camera endoscope at 4 different depths within the bed; the endoscopic ports were specifically designed to provide an appropriate protection for the endoscopes thus minimizing the influence of wall vibration; their special design allowed to precisely positioning the probe providing micro adjustments in all the 3 directions.

2.5 *PIV acquisition and processing*

The flow was seeded with neutrally buoyant, spherical, hollow glass particles ($\rho_p = 1050$ g/cc) with a nominal mean diameter of 11 μm. A single-exposure double-frame PIV approach was used to capture particle images. For the results presented here, an image acquisition rate of 15 Hz was sufficient to prevent aliasing problems, fully characterize the large vortex structure evolution and, maximize the acquisition period in order to obtain representative mean results (about 33 sec).

Image distortion was corrected by use of a calibration target placed in the measurement plane within the pore space prior to experiments taking place. The target consisted of a plate (30*30 mm) with a regular grid of circular dots, spaced 1 mm apart. Image processing based upon application of a threshold was applied to the calibration image and automatic blob analysis algorithms were applied in order to determine the dot's centroid location. A fourth order polynomial function was judged appropriate to mathematically describe the effect of the spherical aberration. In order to correct the image distortion all the collected raw images were dewarped before data interrogation on the basis of the calibration function.

Image interrogation was performed by applying a cross-correlation function to each image pair. A fast Fourier transform (FFT) method was applied to optimize the computation time in locating cross-correlation peaks. A 64*64 pixels interrogation window was used (which corresponds to

an average window size in the range of 1*1 to 1.5*1.5 mm).

In order to remove spurious vectors, statistical validation criteria and local validation algorithms based on neighborhood interrogation methods (Westerweel, 1994) were applied. Application of these techniques resulted in 15-25% of instantaneous vectors being deemed as erroneous and were mainly caused by a localized lack of seeding particles or low illumination. Missing data in the instantaneous flow fields was partially reconstructed using second-order correlation techniques (Hart, 2000) which allowed us to keep the spatial resolution appropriate for the flow structure characterization. The filling algorithms are based on recursive methods starting from data validated with the highest confidence as input and finally applying 2D interpolation functions. Data smoothing was undertaken for instantaneous flow field representation but only fully validated vectors were used for calculation of the mean flow field.

An example of the experimental output is shown in Figure 4, which highlights the circular field of view provided by the endoscopes. As shown in Fig. 4, the E-PIV is able to visualize the entire pore space, capturing important data that would be hidden from external techniques (that portion of the field of view that overlaps the spheres).

3 RESULTS AND DISCUSSION

In this paper we present results from an experiment in which the flow depth was $h_{fsf} = 0.06$ m (which gives a solid-particle diameter to flow-depth ratio of $D/h_{fsf} = 0.67$) while the mean free-stream velocity was $U_0 = 0.568$ m (which gives free-stream Reynolds and Froude number of $Re = 3.4*10^4$ and a $Fr = 0.73$ respectively).
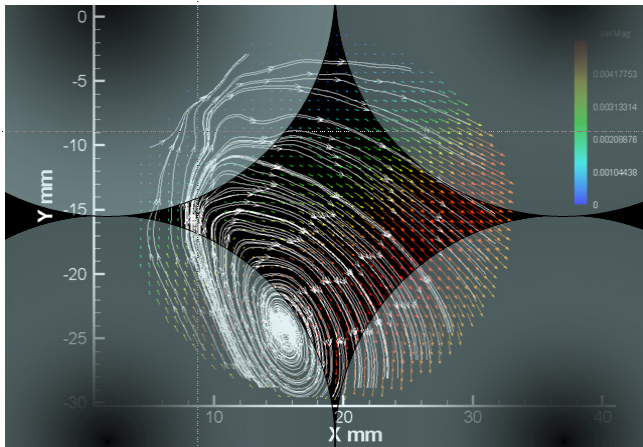
Figure 4. Example of flow field obtained applying the E-PIV within the pore space of a permeable bed.

3.1 *Experimental instantaneous flow structures*

In Figure 5 an example of the instantaneous flow shows that the flow is clearly non-uniform with a high velocity region located close to the upstream inlet. The maximum pore velocity $u_{pmax} = 0.30$ m/s is high and of the same order of magnitude as the mean stream-flow velocity U_0 ($u_{pmax}/U_0 = 0.54$). The high-velocity region represents the front of a jet that penetrates the pore, triggering the formation of the vortical structure with anticlockwise rotation seen in the bottom right sector of the pore.
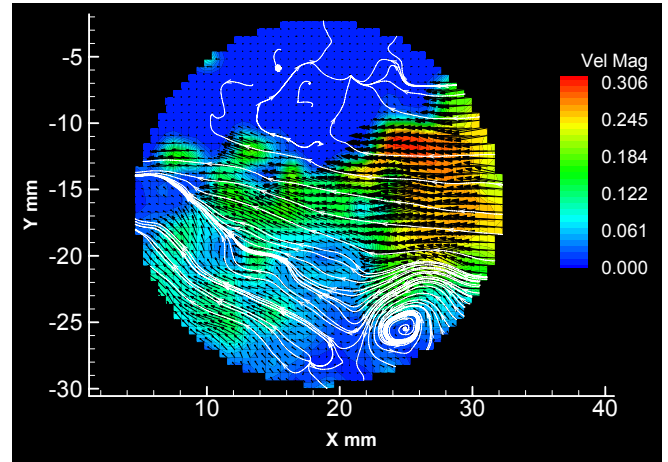
Figure 5. Experimental results of the instantaneous flow within the pore space ($h_{fsf} = 0.06$ m, $U_0 = 0.568$ m, $Re = 3.4*10^4$, $Fr = 0.73$). The colormap refers to velocity magnitude expressed in [m/s].

In Figure 6 evolution of the flow structure is demonstrated by a sequence of eight sequential flow fields representing two similar evolution cycles (the cycle period ~ 0.27 s). Figure 6A and 6E refer to the typical initial step and show the front of a horizontal downstream jet which penetrates into the pore space resulting in three distinct regions within the pore. Each region is characterized by different flow magnitude and direction. The central section of the field of view is mainly occupied by the jet; the flow velocity is relatively high, the flow moves horizontally, according with the jet direction. The lateral regions, located at the edges of the jet are dominated by flow moving orthogonally to the jet at low velocity or rotating according to the jet direction. The instability typical of the transition between the two regions promotes the formation of vortical structures (Kelvin-Helmholtz instability). The early stages of the formation of these vortices can be seen in the lower sections of Figure 6B and 6F where the shear stress provided by the jet results in an anticlockwise rotation. In Figure 6C and 6F the anticlockwise vortices are fully formed and the jet has penetrated the whole pore with a high-velocity region present from right to left. The decay stage of the vortex is shown in Figure 6D and 6G. In this

phase the vortices are pushed downstream and become elongated before finally dissipating.

3.2 *Experimental mean flow field*

The experimental mean flow field was obtained by mapping the time-average velocity over each grid point included in the interrogation area. This method was computationally efficient and hence well suited for processing large amounts of data (Meinhart et al., 2000).

Figure 7 illustrates the distribution of velocity magnitude, total turbulence (computed as standard deviation of the velocity fluctuations), Reynolds stresses and vorticity as averaged over 500 instantaneous flow fields. The velocity magnitude (Figure 7a) shows a central horizontal region which represents the jet penetration path. The highest velocities are concentrated to the right of the field of view, where the jet enters. The flow is relatively symmetric with high velocity at the center and low velocity at the top and bottom of the field of view. It should be noted that the slightly lower velocities recorded at the top of the pore may be due to the difficulty in providing a perfectly uniform illumination to the whole field of view. The flow pattern shows that the fluid coming from the right flows perfectly horizontally in the center of the pore and diverges vertically towards the top and bottom, thus demonstrating the typical behavior of a laterally expanding jet. It is interesting to note that at the bottom of the field of view, the curvature of the streamlines suggests the presence of an elongated rotation, presumably associated with counter-rotating flow at the top of the pore beneath.

Figure 7b shows the presence of high turbulence located at the border between the high-velocity and low-velocity regions described above. This suggests that the energy of the jet dissipates by turbulence momentum exchange between the jet flow and the adjacent low velocity fluid. The pattern of Reynolds stress within the pore (Figure7c) is in agreement with this interpretation. Reynolds stresses are significantly high at the bottom of the field of view where the dissipation mechanisms operate and where formation and advection of large vortical structures are observed. Finally, the vorticity distribution (Figure 7d) also confirms the presence of a predominant horizontal jet flow producing lateral rotation.

3.3 *Numerical mean flow field*

Numerical results are shown in Figure 8 and 9 in term of the distribution of the mean streamwise and wall-normal component respectively. These results confirm the observations described above and show the importance of jet flows penetrating the pore space in setting up the overall flow structure and vortex formation. Figure 8 suggests that the fluid close to the upstream pore (right) moves downstream, similar to that found in the experiments. More specifically, Figure 10 shows a direct comparison between experimental and numerical results extracted from the same location. For the right part of the pore the results agree both in magnitude and direction. However, the numerical simulation suggests that the fluid close to the downstream pore (left) moves resulting in a horizontal convergence of flow towards the pore which was not seen in the experiments. The simulations suggest that the majority of the pore-flow is characterized by a significant unidirectional downward-moving vertical component, while the experiments seem to highlight vertical motion only in the region outside the central horizontal jet. At the lowest part of the pore the vertical component is ~ zero, thus suggesting that the fluid cannot be ejected through the basal outlet. The fluid is presumably ejected in the spanwise direction instead.

Figure 11 shows a direct comparison of the wall-normal velocity component extracted from the same pore of the experiment and numerical simulation. Both the figures seem to suggest the presence of upward moving flow located at the bottom left of the pore. Downward-moving fluid is observed at the bottom-right and top-right segments of the pore in both sets of data, although with different magnitudes.

4 CONCLUSION

In this paper, high-resolution endoscopic PIV data are compared with numerical results for the simple model of a permeable bed made packing uniform size spheres (D = 4 cm) in a cubic arrangement.

Measurements have shown that the flow is dominated by a horizontal jet penetrating into the pore. The instantaneous flow structure within the pore space is strictly related to the characteristics of jet flow entering the pore and to the initial flow conditions within the pore.

The edges of the jet are characterised by intense turbulence activity resulting in velocity fluctuations and the formation of large vortices in the pore space. Vortex formation in the pore space is found to be associated with a Kelvin-Helmholtz type of instability driven by jets.

Preliminary numerical results show to be in good agreement with experimental data. The results confirm the importance of jet flows penetrating the pore space in setting up the overall flow

structure and vortex formation. The main differences are found in the vertical component of velocity which requires further effort. To improve the comparison between the CFD and EPIV data we are currently investigating the free-surface representation. It is felt that the current free-surface approximation in the CFD scheme is not resolving the pressure field as accurately as possible and thus causing differences in velocity predictions within the hyporheic matrix.

REFERENCES

Bencala, K.E. and Walters, R.A. 1983. Simulation of solute transport in a mountain pool-and-riffle stream: a transient storage model. Water Resources Research, 19(3), 718-724.

Hardy, R.J., Lane, S.N., Lawless, M.R., Best. J.L. Elliot, L. and Ingham, D.B. 2005. Development and testing of numerical code for treatment of complex river channel topography in three-dimensional CFD models with structured grids. Journal of Hydraulic Research, 43(5), 468-480.

Hart, D.P. 2000. PIV error correction. Experiments in Fluids, 29, 13-22.

Lage, J.L., Lemos, M.J.S. and Nield, D.A. 2002. Modelling turbulence in porous media In: Transport Phenomena in Porous media 2. Eds DB Ingham & I Pop Elsevier, 198-232.

Lane, S.N., Hardy, R.J. Elliot, L., and Ingham, D.B. 2003. High resolution numerical modelling of three dimensional flows over complex river bed topography. Hydrological Processes, 16, 2261-2272.

Lane, S.N., Hardy, R.J., Elliot, L. and Ingham, D.B. 2004. Numerical modelling of flow processes over gravelly-surfaces using structured grids and a numerical porosity treatment. Water Resources Research, (40) W01302, DOI:10.1029/2002WR001934.

Meinhart, C. D., Wereley, S. T., Santiago, J. G. 2000. A PIV algorithm for estimating time-averaged velocity fields. Journal of Fluids Engineering, 122, 285-289, DOI: S0098-2202(00)00602-7.

Patankar, S.V. and Spalding, D.B. 1972. A calculation procedure for heat, mass and momentum transfer in three-dimensional parabolic flows. International Journal of Heat and Mass Transfer, vol. 15, 1787-1806.

Raudkivi, A.J. 1998. Loose boundary Hydraulics A.A. Balkema, Rotterdam.

Westerweel, J. 1994. Efficient detection of spurious vectors in particle image velocimetry data. Experiments in Fluids, 16, 236-247.
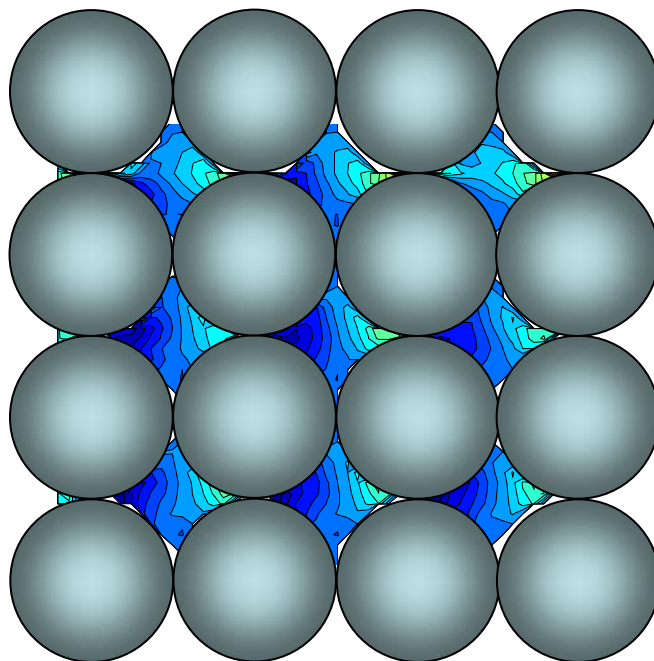
Figure 8. Numerical simulation showing the distribution of the mean wall-normal velocity component.
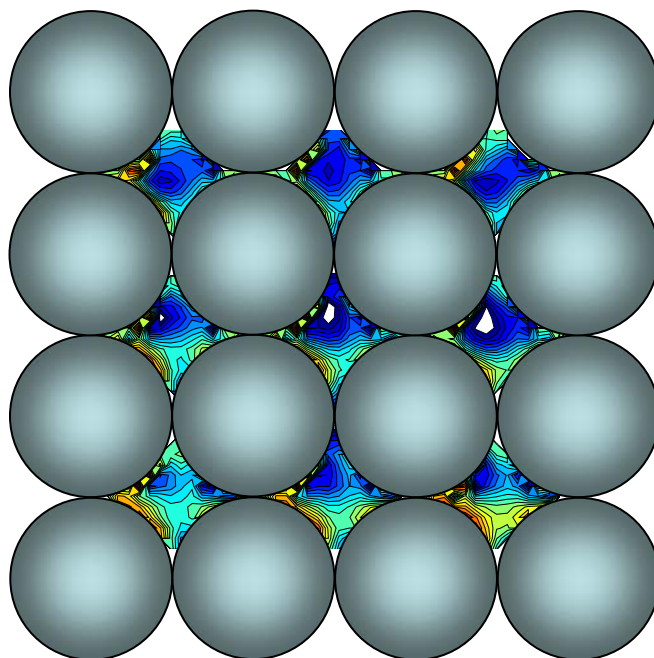

Figure 9. Numerical simulation showing the distribution of the mean wall-normal velocity component.
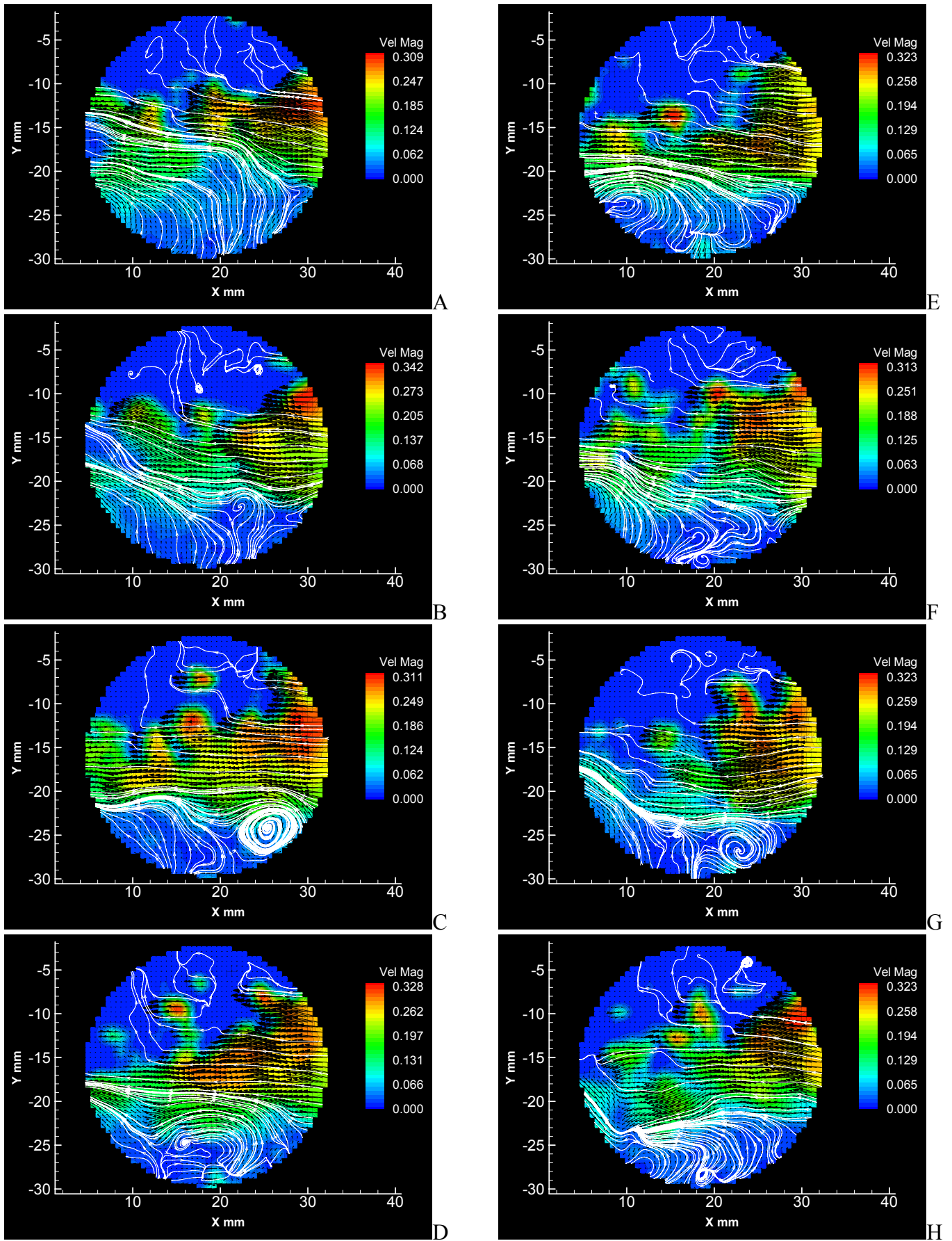
Figure 6. Experimental data showing a sequence of instantaneous flow fields (within the pore space) obtained with a frame repetition rate = 15 Hz (h_{fsf} = 0.06 m, U_0 = 0.568 m, Re = 3.4*10^4, Fr = 0.73). The colormap refers to velocity magnitude expressed in [m/s].
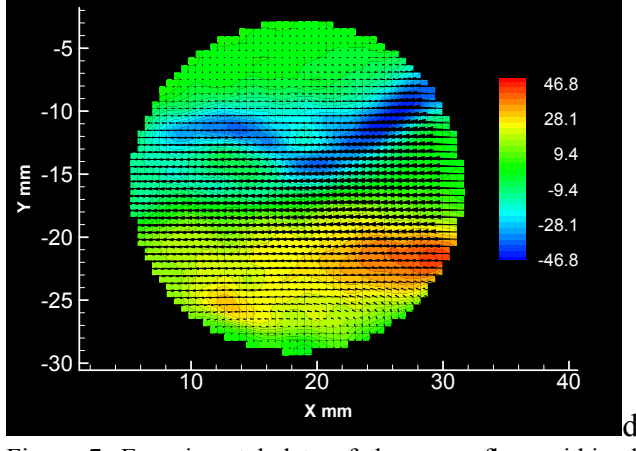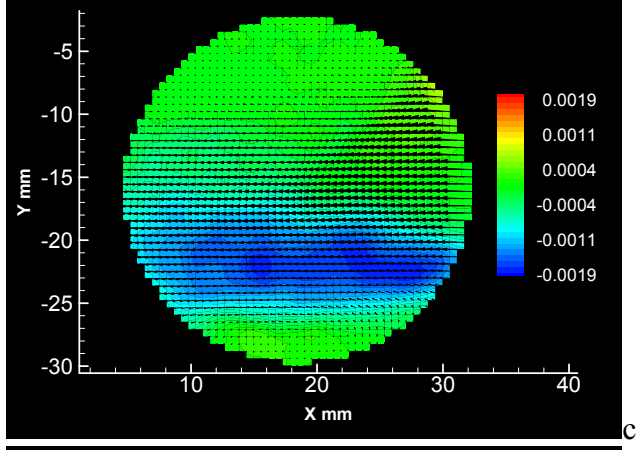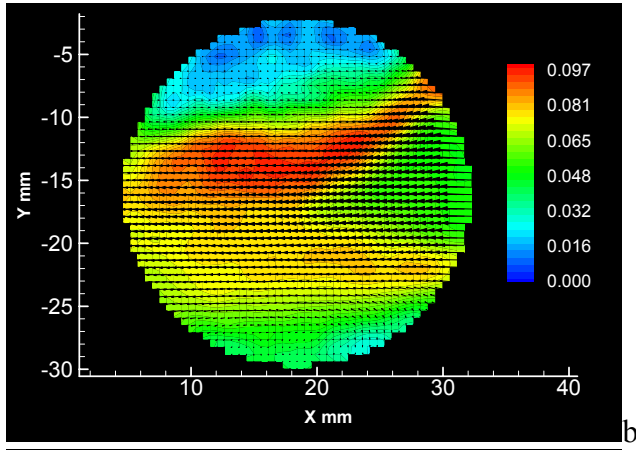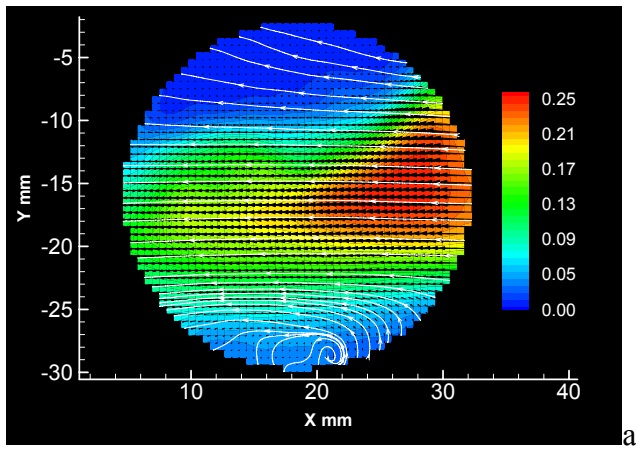
Figure 7. Experimental data of the mean flow within the pore space ($h_{fsf} = 0.06$ m, $U_0 = 0.568$ m, Re $= 3.4*10^4$, Fr $= 0.73$). Distribution of: a) velocity magnitude; b) turbulence (std); c) Reynolds stresses; c) vorticity.
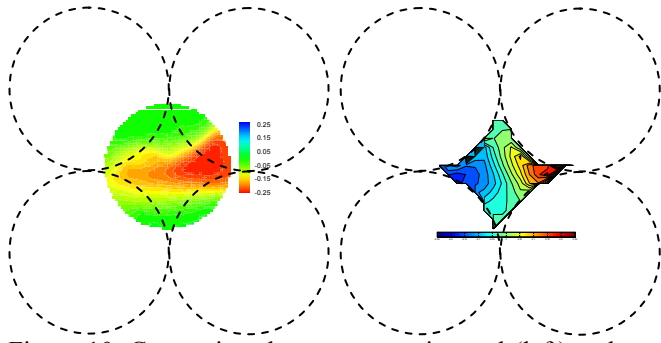

Figure 10. Comparison between experimental (left) and numerical (right) streamwise component distribution within the pore space.
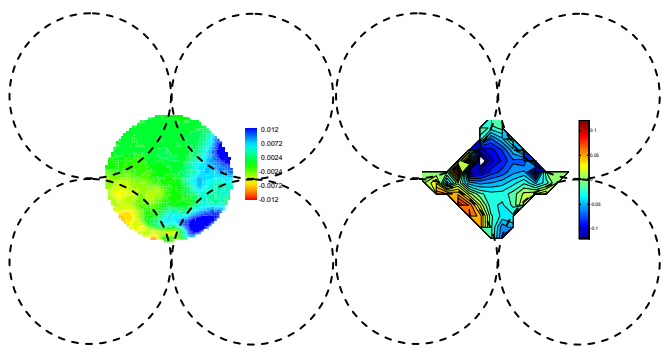

Figure 11. Comparison between experimental and numerical wall-normal component distribution within the pore space.